



Microwave properties of Ba_{0.5}Sr_{0.5}TiO₃ thin film coplanar phase shifters

P. M. Suherman, T. J. Jackson, Y. Y. Tse, I. P. Jones, R. I. Chakalova et al.

Citation: *J. Appl. Phys.* **99**, 104101 (2006); doi: 10.1063/1.2198933

View online: <http://dx.doi.org/10.1063/1.2198933>

View Table of Contents: <http://jap.aip.org/resource/1/JAPIAU/v99/i10>

Published by the [American Institute of Physics](#).

Additional information on *J. Appl. Phys.*

Journal Homepage: <http://jap.aip.org/>

Journal Information: http://jap.aip.org/about/about_the_journal

Top downloads: http://jap.aip.org/features/most_downloaded

Information for Authors: <http://jap.aip.org/authors>

ADVERTISEMENT



**FIND THE NEEDLE IN THE
HIRING HAYSTACK**

Post jobs and reach
thousands of hard-to-find
scientists with specific skills



<http://careers.physicstoday.org/post.cfm> **physicstoday** JOBS

Microwave properties of $\text{Ba}_{0.5}\text{Sr}_{0.5}\text{TiO}_3$ thin film coplanar phase shifters

P. M. Suherman,^{a)} T. J. Jackson, Y. Y. Tse, I. P. Jones, R. I. Chakalova, and M. J. Lancaster
School of Engineering, University of Birmingham, Edgbaston, Birmingham, B15 2TT, United Kingdom

A. Porch
School of Engineering, Cardiff University, CF24 3AA, United Kingdom

(Received 11 July 2005; accepted 28 March 2006; published online 23 May 2006)

Coplanar waveguide transmission lines have been used to show that the temperature dependent properties of $\text{Ba}_{0.5}\text{Sr}_{0.5}\text{TiO}_3$ thin films used for microwave phase shifters in the frequency range 45 MHz–50 GHz are correlated strongly with the microstructure of the films. The highest tunability and figure of merit of the phase shifters were obtained for films with the narrowest ferroelectric-paraelectric phase transition range, lowest mosaic spread, and widest columnar microstructure. The study also showed that the operating temperature plays an important role in achieving the optimum phase shift for microwave applications. © 2006 American Institute of Physics. [DOI: 10.1063/1.2198933]

I. INTRODUCTION

As materials which can produce frequency agility in microwave applications, ferroelectrics have been investigated widely in recent years. Applications such as phase shifters, variable frequency resonators, steerable antennas, and tunable filters have all been developed.^{1,2} All these applications utilize the strong dependence of the permittivity on the application of a dc-bias voltage. An ideal ferroelectric for microwave device applications should result in high tunability and have both low dielectric loss and a reasonably large value of permittivity (>100). All of these factors are affected by the film fabrication conditions and the resulting microstructure. In this work, we investigate the dielectric properties over a very wide range of microwave frequencies (45 MHz–50 GHz), rather than at the lower, narrower frequency ranges (<10 GHz) more commonly studied.^{3–5} The material investigated is $\text{Ba}_{0.5}\text{Sr}_{0.5}\text{TiO}_3$, which has a Curie temperature (T_c) around room temperature.

Sections II and III describe the methods of device preparation and characterization. The microstructural and microwave properties of the ferroelectric films are considered in Sections IV A and IV B, respectively, and a phase shifter is evaluated in Sec. IV C.

II. SAMPLE PREPARATION

$\text{Ba}_{0.5}\text{Sr}_{0.5}\text{TiO}_3$ (BST) thin films were deposited onto (001) MgO substrates (of thickness 0.5 mm) by pulsed laser deposition, using a laser fluence of 1.5 J cm^{-2} at 5 Hz pulse rate in the presence of an oxygen gas background. During deposition, the substrate temperature was 750°C . In separate depositions, oxygen pressures of 10^{-4} to 10^{-1} mbar were chosen to vary the films' crystallinity and resulting microwave properties. The films were grown to a thickness measured to be 300 nm–400 nm. Two types of post-deposition annealing were investigated. *In situ* annealing was carried

out directly in the chamber at 650°C under static O_2 for 1 h at ~ 800 mbar. *Ex situ* annealing was carried out in a flowing O_2 furnace for 24 h at 1150°C . Silver coplanar waveguide (CPW) transmission lines 300 nm thick, with a center-line width ($2s$) of $50 \mu\text{m}$ and gap width (g) of $25 \mu\text{m}$, were patterned onto the ferroelectric films by lift-off photolithography (Fig. 1). Various lengths of transmission lines (450, 900, 1800, 3500, and $5250 \mu\text{m}$) were fabricated.

III. EXPERIMENTAL METHOD

A. Microstructural properties

The crystalline properties of the films were characterized using a six-circle x-ray diffractometer with $\text{CuK}\alpha$ radiation. The following measurements were made to examine epitaxial growth and crystallinity:

- (1) Symmetric $\theta/2\theta$ scans of the planes parallel to the film surface.
- (2) Asymmetric (decoupled) ω - 2θ scans at $\{hkl\}$ reflections of (001), (002), (004), (303), (033), (013), (113), (123), (224), (024). The in-plane and out-of-plane lattice parameters were determined by least squares fitting using Cohen's method.⁶
- (3) ϕ scans on (013) and (113) reflections for substrate and film, respectively, to determine the in-plane epitaxial orientations.
- (4) ω scans at (002) reflections for both substrate and films, to characterize the "mosaic" spread expressed as full width half at maximum (FWHM).

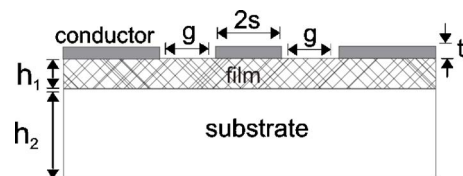


FIG. 1. Schematic diagram of the silver coplanar waveguide transmission line patterned on the ferroelectric thin film and its MgO substrate.

^{a)}Author to whom correspondence should be addressed; electronic mail: m.suherman@bham.ac.uk

TABLE I. Cell parameters of films deposited at various oxygen pressures and annealed *in situ*.

Oxygen Pressure (mbar)	FWHM (°)	In-plane cell parameter (Å)	Out-of-plane cell parameter (Å)	Strain of the in-plane cell parameter (%)	Strain of the out-of-plane cell parameter (%)
3×10^{-1}	0.48	3.96246 ± 0.00311	3.96664 ± 0.00239	0.2378	0.3415
10^{-1}	0.8657	3.95896 ± 0.00152	3.94851 ± 0.00119	0.1482	-0.1161
10^{-2}	1.1198	3.96013 ± 0.00312	3.99416 ± 0.00258	0.1771	1.0397
10^{-3}	1.0873	3.96438 ± 0.00468	3.99389 ± 0.00386	0.2859	1.0321
10^{-4}	0.9363	3.97569 ± 0.00384	3.99542 ± 0.00315	0.5717	1.0700

The surface morphology was analyzed using atomic force microscopy (AFM), while the cross section of the films was investigated using transmission electron microscopy (TEM). The chemical composition of the films was confirmed using energy dispersive x-ray analysis (EDX) in a scanning electron microscope.

B. Microwave properties

Microwave measurements (45 MHz–50 GHz) were performed from 80 K–360 K using a cryogenic probe station with ground-signal-ground probes connected to a vector network analyzer. A bias-tee was used to apply bias voltages of 0 V to ± 90 V between the ground and signal lines, producing electric fields between 0 to ± 3.6 V μm^{-1} . Calibration to the probe tips was carried out using the LRRM (load-reflect-reflect-match) method using impedance standards formed from gold CPW lines on an alumina substrate. The LRRM calibration technique requires four standard measurements, of which only the 50 Ω matched load and thru (delay) need to be known precisely. The reflection measurements are made with the probes lifted off the substrate and with the probes placed on a shorted line.

The complex propagation constant ($\gamma = \alpha + i\beta$) defining microwave propagation on the transmission lines was calculated from the scattering parameters (amplitude and phase of return loss S11, S22 and insertion loss S21, S12) obtained from the microwave measurements via ABCD parameters.⁷ α is the attenuation constant and β is the phase constant. The attenuation constant α involves both dielectric (α_d) and conductor losses (α_c). The effective permittivity of the coplanar transmission line was calculated from

$$\epsilon_{eff} = - \left(\frac{c_0 \gamma}{2\pi f} \right)^2, \quad (1)$$

where c_0 is the speed of light in a vacuum and f is the measurement frequency. The real part of permittivity of the film (ϵ') was obtained from the conformal mapping method for coplanar waveguide transmission lines,⁸ from which the following result is obtained:

$$\epsilon' = \frac{1}{q_1} [(2\epsilon'_{eff}) - (q_2 \epsilon_s) + q_2 - 2 + (q_1 \epsilon_s)]. \quad (2)$$

In Eq. (2), ϵ_s is the permittivity of the substrate (assumed to be purely real, appropriate for a very low loss substrate such as MgO), ϵ'_{eff} is the real part of effective permittivity, and q_1 and q_2 are geometrical factors involving the transmission line

dimensions, the thickness of the film and thickness of the substrate. These geometrical factors may be written analytically for arbitrary geometries in terms of an elliptic integral of the first kind, but for a very thin film, the geometrical factor q_1 may be determined using the approximation given in Ref. 1.

Before applying this analysis method to deduce the dielectric properties of our ferroelectric films, it was first verified for silver coplanar waveguide transmission lines patterned onto bare MgO and LaAlO₃ (LAO) substrates.⁹ Results for the relative permittivity of the substrates comparable with the expected, well-established values were obtained, with error less than 1% ($\epsilon_{\text{MgO}} \approx 9.5$; $\epsilon_{\text{LAO}} \approx 24$).

In this work we present the losses as an effective loss tangent ($\tan \delta_{eff}$). This involves both dielectric (α_d) and conductor (α_c) losses and is obtained from expression

$$\tan \delta_{eff} = \frac{\epsilon''_{eff}}{\epsilon'_{eff}}, \quad (3)$$

where ϵ'_{eff} and ϵ''_{eff} are real and imaginary parts of effective permittivity, respectively.

IV. RESULTS AND DISCUSSION

A. Microstructural properties

X-ray diffraction scans showed that the BST films were of single phase with (00 l) orientation, confirming that epitaxial growth had taken place. Table I shows data for films annealed *in situ*. The in-plane and out-of-plane lattice parameters, strain determined from the lattice parameters of the target (3.9531 Å), and the full width half maximum (FWHM) of rocking curves of the (002) diffraction peaks are given. The films grown at high pressure tended to be cubic at room temperature, whereas the films grown at low pressure tended to be tetragonal. For low pressure deposition, the out-of-plane lattice parameters had greater expansion compared with the in-plane lattice parameter. The expanded out-of-plane lattice parameter of films grown at low pressure may be indicative of greater structural disorder or of increased oxygen vacancies.

EDX measurements showed that the composition of all the films grown at various pressures was consistent with the commercially nominal stoichiometry of the target to within an error of 0.5%.

The cross-sectional TEM pictures revealed a columnar structure for all *in situ* annealed films irrespective of deposition pressure, with a column width ~ 50 nm [Fig. 2(a)]. EDX

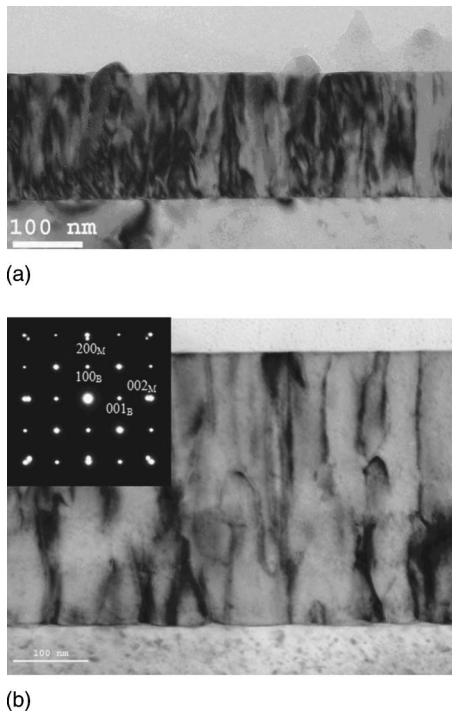


FIG. 2. TEM cross section of film fabricated at 10^{-1} mbar oxygen pressure with (a) *in situ* annealing, (b) *ex situ* annealing. “M” refers to MgO, “B” refers to BSTO.

analysis in the TEM (spot size was set to 2 nm at an accelerating voltage of 200 kV) showed no significant difference in the atomic composition across the columnar boundaries within an error of 0.4%. However, the annealing process had a significant effect, such that *ex situ* annealed films possessed a wider columnar structure ranging from 80 to 120 nm as compared with the *in situ* annealed films [Fig. 2(b)]. This trend was confirmed by the AFM images of the surface morphology of the films. From the high order electron diffraction spot [inset of Fig. 2(b)], the lattice misfit was estimated to be 6.2% in the *ex situ* annealed film. This is consistent with the result based on the lattice parameters of BSTO and MgO. This indicates that the strain is fully relaxed at the interface by misfit dislocations between the film and the substrate.

AFM showed that *in situ* annealed films had a very smooth surface (rms roughness ~ 0.5 nm), with a grain size of about 50 nm. After *ex situ* annealing, small crystallites were observed which were coincident with the column boundaries. Between these crystallites, the grain size had increased to ~ 124 nm and the surface roughness reduced to ~ 0.25 nm. The crystallites were about 5 nm high and 30 nm in diameter. The shape and size of the grains shown in AFM

TABLE II. Effect of annealing on films deposited at 10^{-1} mbar oxygen pressure.

	<i>In situ</i> Annealing	<i>Ex situ</i> Annealing
FWHM ($^{\circ}$)	0.8657	0.2654
In-plane cell parameter (\AA)	3.95896 ± 0.00152	3.96033 ± 0.00095
Out-of-plane cell parameters (\AA)	3.94851 ± 0.00075	3.95549 ± 0.00075

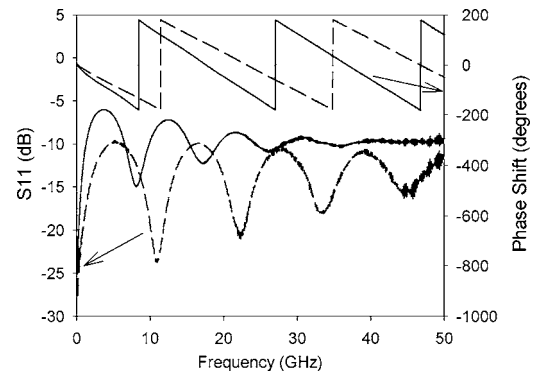


FIG. 3. Magnitude of return loss ($|S_{11}|$) and phase shift ($\arg S_{12}$) of a silver coplanar waveguide on BST/MgO film deposited at 10^{-1} mbar and annealed *ex situ*. Data is shown for electric field biases of 0 (solid line) and 3.2 $\text{V } \mu\text{m}^{-1}$ (dashed line).

are consistent with the columnar microstructure observed by TEM cross section.

The annealing process also produced a considerable change in the crystalline properties of the films. Table II shows the effect of annealing on samples deposited at 10^{-1} mbar oxygen pressure. *Ex situ* annealed samples showed a smaller mosaic spread by almost 60%. The in-plane cell parameters were the same within error bars for both *in situ* and *ex situ* annealed films and the out-of-plane lattice parameter was slightly increased with *ex situ* annealing.

B. Microwave properties

Typical scattering parameter data obtained from microwave measurements on $\text{Ba}_{0.5}\text{Sr}_{0.5}\text{TiO}_3$ films on MgO substrates are shown in Fig. 3.

The real part of the dielectric permittivity ϵ' of *ex situ* annealed BST films was typically ~ 1800 at 0 V and almost constant in the broadband frequency range up to 50 GHz (Fig. 4). An apparent rapid increase of permittivity at frequency < 3 GHz, as shown in Fig. 4, is due to the larger inductance at frequencies lower than $f = 1/(\mu_0 \sigma t_s)$. The conformal mapping used to calculate the permittivity is valid at frequencies $f > 1/(\mu_0 \sigma t_s)$, or when $t_s < \pi \delta_c^2$; μ_0 is permeability of free space, σ is conductivity of the metalization, t

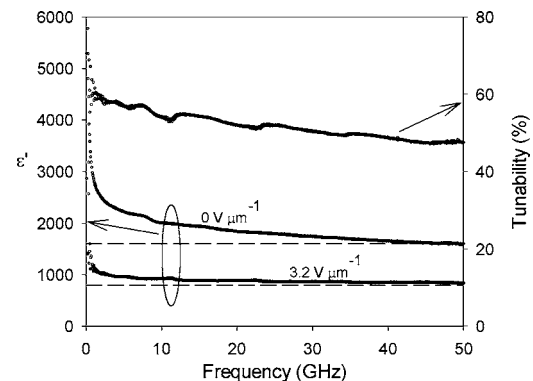


FIG. 4. Real part of the permittivity of a film deposited at 10^{-1} mbar and annealed *ex situ*. 50% tunability was obtained between 0 and 3.2 $\text{V } \mu\text{m}^{-1}$ electric field bias. The dashed lines show the permittivity calculated from the time domain measurement.

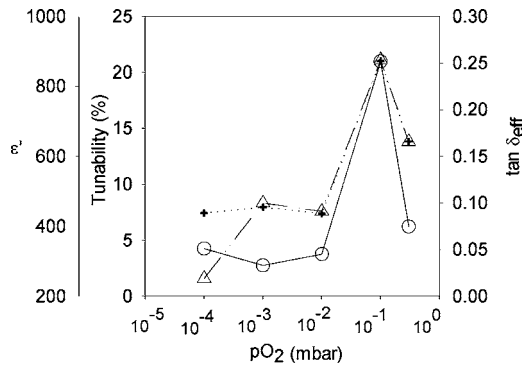


FIG. 5. Tunability (O), effective dielectric loss tangent (+), and permittivity (Δ) of *in situ* annealed films deposited at various oxygen pressures. Data at 20 GHz and $1.6 \text{ V } \mu\text{m}^{-1}$ are shown.

is metal thickness, δ_c is the skin depth, and s is half of the center-width of CPW.^{10,11} For transmission lines 300 nm thick, with $s=25 \mu\text{m}$, and conductivity $\sigma=3.7 \times 10^7 \text{ S/m}$ obtained from van der Pauw measurements, the frequency limit is confirmed as $f > 3 \text{ GHz}$.

If the permittivity is assumed to be independent of frequency, it can be determined directly from the propagation delay for signals launched onto the transmission lines. This delay was obtained from time domain analysis of S12.¹² The real part of the effective dielectric permittivity was then calculated from Eq. (4),

$$\epsilon'_{eff} = - \left(\frac{c_0 t_l}{l} \right)^2, \quad (4)$$

where t_l and l are delay time and length of the transmission line, respectively. The data calculated from this delay time was comparable with that derived previously, as shown in Fig. 4.

The permittivity of the films was strongly dependent on the oxygen pressure during deposition. Figure 5 shows the real dielectric permittivity ϵ' , tunability at $1.6 \text{ V } \mu\text{m}^{-1}$ and effective dielectric loss measured at 20 GHz for *in situ* annealed films. The tunability of the films is defined as

$$\text{Tunability} = \frac{\epsilon'(V) - \epsilon'(0)}{\epsilon'(0)} 100\%, \quad (5)$$

where $\epsilon'(V)$ and $\epsilon'(0)$ are real parts of the permittivity at dc-bias voltage V and 0 Volts, respectively.

Films grown in an oxygen pressure of 10^{-1} mbar with the other parameters set as described in Sec. II reproducibly had the highest tunability. Films grown at 10^{-1} mbar had the smallest cell parameters and tended to have a cubic structure rather than tetragonal. This lower permittivity of *in situ* annealed films deposited at lower oxygen pressure seems to be due to the mechanical strain and oxygen defects.

After *ex situ* annealing, films deposited at 10^{-1} mbar did not show any improvement in tunability. However, *ex situ* annealing greatly increased the tunability of films deposited at 10^{-4} mbar as shown in Fig. 6. The tunability was increased by $\sim 30\%$ compared with the *in situ* annealed films.

Figure 7 shows the $\epsilon'(E)$ curve for measurement at 80 K and 300 K of films fabricated at 10^{-1} mbar oxygen pressure and annealed *ex situ*. The $\epsilon'(E)$ curve is equivalent to a

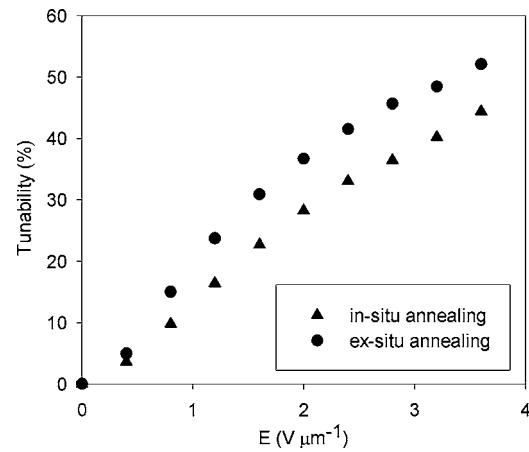


FIG. 6. Comparison of the tunability of films annealed *in situ* and *ex situ* as a function of electric bias field.

capacitance-voltage curve in low frequency studies. There was no hysteresis at 300 K but hysteresis was observed at 80 K.

While films deposited at 10^{-1} mbar oxygen pressure did not show significant hysteresis at 300 K, films deposited at 10^{-1} mbar oxygen pressure showed pronounced hysteresis at the same temperature. This suggested that films deposited at 10^{-1} mbar oxygen pressure were in the paraelectric state at room temperature while films deposited at 10^{-1} mbar oxygen pressure were in the ferroelectric state despite the *ex situ* annealing.

The temperature dependence of $\epsilon'(E)$ of a film deposited at 10^{-1} mbar and annealed *ex situ* are shown in detail in Fig. 8. Figure 8 shows data for dc-bias voltages from 0 to 90 V. The permittivity shows a broad maximum at temperature T_{max} which increases with bias voltage. This T_{max} is not expected to be equal to Curie temperature T_c . In order to find T_c , the inverse of real permittivity was plotted against temperature as shown in Fig. 9. T_c was found to be 225 K from the temperature intercept of the straight line fitted to data above T_{max} . This is in reasonable agreement with the value expected for bulk material. The value of T_c was seen to decrease with increasing bias voltage. A value for the Curie-

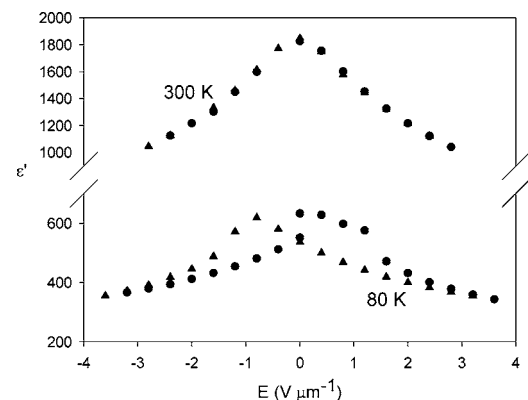


FIG. 7. $\epsilon'(E)$ curve of an *ex situ* annealed film deposited at 10^{-1} mbar oxygen pressure. \blacktriangle and \bullet represent the permittivity when voltage was swept up and down, respectively in order to demonstrate any hysteresis behavior.

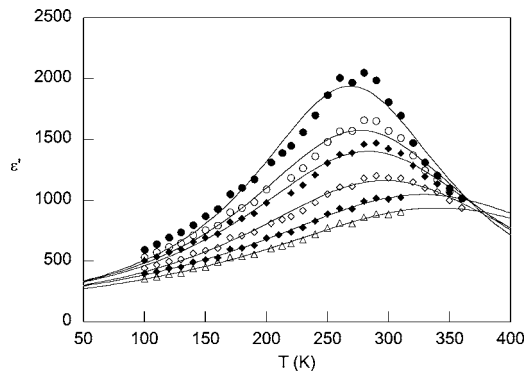


FIG. 8. Temperature dependent permittivity ϵ' of a film deposited at 10^{-1} mbar and annealed *ex situ*. Data are shown at bias voltages, from top to bottom, of 0, 20, 30, 50, 70, and 90 V. The solid lines are fits to Smolenski's expression.

Weiss constant, $\theta_c = 1.28 \times 10^5$ K, was determined from the slope of the data in Fig. 9 according to

$$\frac{1}{\epsilon'} = \frac{1}{\epsilon_0} \frac{T - T_c}{\theta_c}. \quad (6)$$

This is in good agreement with values published elsewhere.^{13,14}

T_{\max} was sensitive to the annealing process and oxygen pressure during film fabrication (Fig. 10). Films grown at the optimal 10^{-1} mbar showed a lower T_{\max} when annealed *ex situ* compared with those annealed *in situ*. The highest T_{\max} was obtained for films grown at 10^{-1} mbar and annealed *in situ*.

The broad transitions to the ferroelectric state shown in Figs. 8 and 10 are indicative of heterogeneous films and therefore the dependences of T_{\max} and T_c on applied voltage are not taken as indicative of the order of the ferroelectric-paraelectric phase transition. The solid lines in Figs. 8 and 10 are fits of Smolenski's description¹⁷ of diffuse ferroelectric transitions, Eq. (7), to the data,

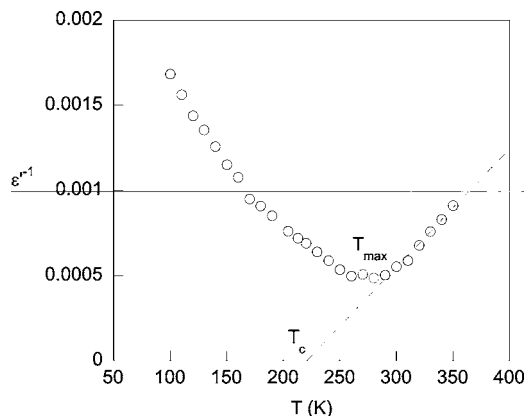


FIG. 9. Temperature dependent of $1/\epsilon'$ at zero bias for a film deposited at 10^{-1} mbar and annealed *ex situ*. The dashed lines are fits to the data at below T_c to determine the Curie-Weiss constant.

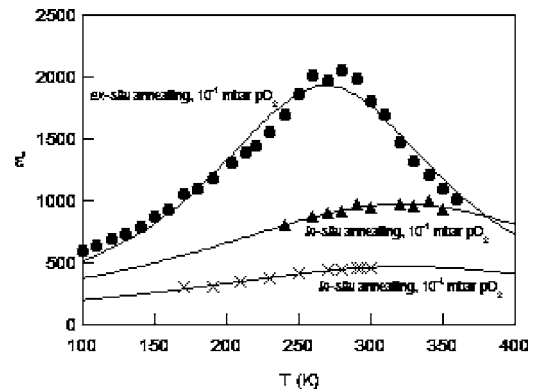


FIG. 10. Temperature dependent permittivity ϵ' at zero bias for various deposition and annealing conditions.

$$\epsilon = \left(\frac{1}{\epsilon_{\max}} + \frac{(T - T_{\max})^2}{2\epsilon_{\max}\xi^2} \right)^{-1}. \quad (7)$$

Equation (7) is frequently used to describe the behavior of relaxor ferroelectrics measured at lower frequency (100 Hz–10 MHz) (Refs. 15–17) but the derivation does not require any particular frequency dependence. The parameter ξ , which quantifies the “diffuseness” of the transition, increases linearly with bias field. A similar increase in diffuseness with bias was reported for $\text{Sr}_{1-x}\text{Ba}_x\text{Nb}_2\text{O}_3$.¹⁸ An increasing ξ suggests an increase in disorder within the sample, or equivalently a widening of a distribution of Curie temperature or permittivity. Considering first the disorder, we might imagine that in zero-field bias, dipole moments are oriented in a direction other than parallel to the plane of the film. In these transmission line structures, the bias field is principally parallel to the plane of the film. An increase in bias field will reorient some of the dipoles and cause an increase of disorder. Considering a distribution of dielectric properties, we might associate the regions with different permittivity as inter- and intracolumnar regions.¹⁹ If the dependence of permittivity on electric field is different in these two regions, then the bias field will broaden the distribution of permittivity within the whole sample. A third interpretation of the increase in ξ is that the applied bias field increases the distribution of built-in electric field and strains generated by charged defects.^{13,14} This will be considered in a later paper.

The effective loss tangent $\tan \delta_{\text{eff}}$ of the same film as in Figs. 8 and 9 is shown as a function of temperature in Fig. 11. The peak in $\tan \delta_{\text{eff}}$ coincides with the peak in permittivity. The electric field bias lowers and broadens the peak in $\tan \delta_{\text{eff}}$ so severely that it is impossible to say if the temperature of the peak moves significantly (outside the error bars). This $\tan \delta_{\text{eff}}$ contains contributions from both conductor (α_c) and dielectric losses (α_d). The conductor loss is linearly proportional to the temperature dependent line resistance and proportional to the square root of the line capacitance, which involves the permittivity of the film, thus creating a distinct peak in $\tan \delta_{\text{eff}}$.

C. Coplanar phase shifters

A typical example of the insertion loss of coplanar phase shifters formed from the films deposited at various oxygen

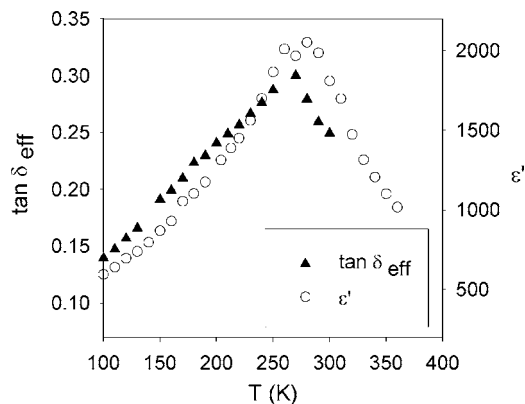


FIG. 11. Temperature dependent permittivity ϵ' and effective dielectric loss, $\tan \delta_{eff}$, of a film deposited at 10^{-1} mbar and annealed *ex situ*.

pressures is shown in Fig. 12. This insertion loss involves both conductor loss from the silver transmission lines (α_c) and dielectric loss from the film itself (α_d). As shown in Fig. 12(a), films deposited with lower oxygen pressure have lower insertion loss, consistent with the lower $\tan \delta_{eff}$ seen in Fig. 5. However, the performance of phase shifters is quantified by a figure of merit, obtained from the ratio of the differential phase shift to the insertion loss [Eq.(8)],

$$\text{Figure of Merit} = \frac{\varphi(V) - \varphi(0)}{IL}. \quad (8)$$

In Eq. (8), $\varphi(V)$ and $\varphi(0)$ are phases ($^\circ$) at dc-bias voltages V and 0 Volts, respectively and IL is the total insertion loss at 0 Volt. The figure of merit expresses the trade-off between tunability and losses. Films deposited at 10^{-1} mbar oxygen pressure had the highest loss, but also the highest differential phase shift [Fig. 12(b)] and hence the highest figure of merit. *Ex situ* annealing for films grown at 10^{-1} mbar oxygen pressure improved the phase shift and figure of merit further (Fig. 13), producing the best phase shifter performance.

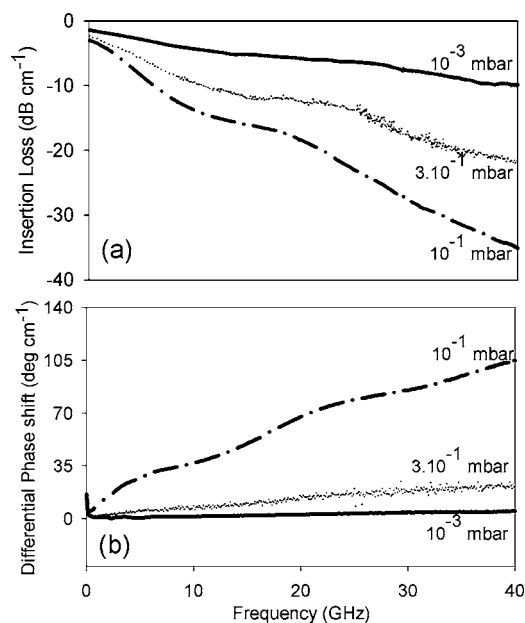


FIG. 12. (a) Insertion loss and (b) differential phase shift per unit length, for films deposited at various oxygen pressures.

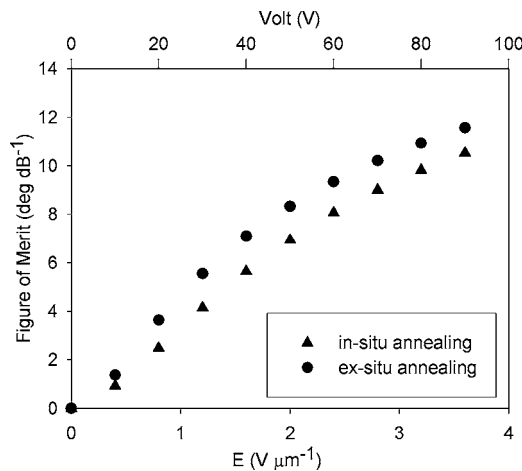


FIG. 13. Figure of merit of coplanar phase shifters established on films deposited at 10^{-1} mbar and annealed *in situ* and *ex situ*.

Figure 14 shows the temperature dependence of tunability and figure of merit of a phase shifter, the maximum values are around T_{max} .

V. CONCLUSION

The temperature dependent microwave properties of $\text{Ba}_{0.5}\text{Sr}_{0.5}\text{TiO}_3$ thin films have been investigated, utilizing a coplanar waveguide transmission line which also functions as a phase shifter. The tunability and figure of merit of the phase shifter are optimized at the temperature T_{max} , where permittivity reaches a maximum. It should be noted that the phase shifters established here are not of an optimal design. For example, a narrower gap would improve the tunability and figure of merit. The insertion loss would be reduced if a thicker conductor were used.

The microwave properties of the film and performance of the phase shifter are strongly correlated with the microstructure of the film. The sharpest ferroelectric-paraelectric transition, the highest tunability, and the largest figure of merit are all obtained for films with the lowest mosaic spread, smallest strain, and widest columnar microstructure.

Three different interpretations of the increase in diffuseness of the ferroelectric-paraelectric phase transition have been suggested. Such models can be tested in the following ways: (1) performing comparative measurements in microstrip and coplanar geometries and using transmission lines

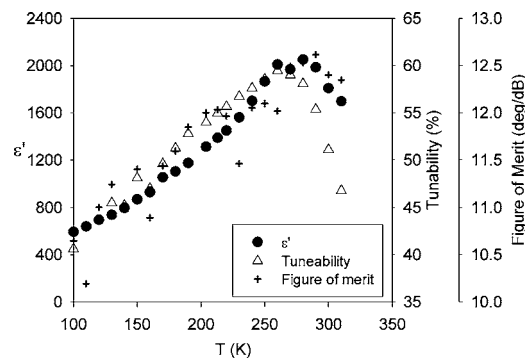


FIG. 14. Temperature dependent permittivity ϵ' (●), tunability (Δ), and figure of merit (+) for a film deposited at 10^{-1} mbar and annealed *ex situ*.

with different gap widths to elucidate the role of the direction of the electric bias field, (2) making changes in deposition parameters sufficiently to suppress columnar growth,²⁰ and (3) employing temperature dependent XRD characterization in the presence of a bias field to measure any internal strain distributions.¹⁹

ACKNOWLEDGMENTS

This work was supported by the UK Engineering and Physical Science Research Council. The authors also wish to acknowledge the assistance of Donna Holdom for sample lithography; and Kenny Leong and Jim Booth from NIST, USA, for discussions and some simulations.

¹M. J. Lancaster, J. Powell, and A. Porch, *Supercond. Sci. Technol.* **11**, 1323 (1998).

²D. S. Kim, Y. Choi, M. O. Allen, J. S. Kenny, and D. Kiesling, *IEEE Trans. Microwave Theory Tech.* **50**, 2903 (2002).

³W. Chang, J. S. Horwitz, A. C. Carter, J. M. Pond, S. W. Kirchoefer, C. M. Gilmore, and D. B. Chrisey, *Appl. Phys. Lett.* **74**, 1033 (1999).

⁴S. Delprat, M. Ouddari, F. Vidal, M. Chaker, and K. Wu, *IEEE Microw. Wirel. Compon. Lett.* **13**, 211 (2003).

⁵S. Hyun, J. H. Lee, S. S. Kim, K. Char, S. J. Park, J. Sok, and E. H. Lee,

Appl. Phys. Lett. **77**, 3084 (2000).

⁶B. D. Cullity, *Elements of X-ray Diffraction*, 2nd ed. (Addison-Wesley, Reading, MA, 1978).

⁷D. M. Pozar, *Microwave Engineering*, 2nd ed. (Wiley & Sons, New York, 1998).

⁸S. S. Gevorgian, *Electron. Lett.* **30**, 1236 (1994).

⁹P. M. Suherman, T. J. Jackson, Y. Koutsonas, R. A. Radoslav, and M. J. Lancaster, *Integr. Ferroelectr.* **61**, 133 (2004).

¹⁰S. Gevorgian, H. Berg, H. Jacobsson, and T. Lewin, *IEEE Microw. Mag.* **4**, 60 (2003).

¹¹S. Gevorgian, T. Martinsson, A. Deleniv, E. Kollberg, and I. Vendik, *IEE Proc., Part H: Microwaves, Antennas Propag.* **144**, 145 (1997).

¹²Agilent Technologies 8510C Network Analyzer System—Operating and Programming Manual, Part No. 08510-90281, Edition 3.0, USA (2001).

¹³O. G. Vendik, S. P. Zubko, and M. A. Nikol'ski, *J. Appl. Phys.* **92**, 7448 (2002).

¹⁴O. G. Vendik and S. P. Zubko, *J. Appl. Phys.* **88**, 5343 (2000).

¹⁵A. Lookman, R. M. Bowman, J. M. Gregg, J. Kut, S. Rios, M. Dawber, A. Ruediger, and J. F. Scott, *J. Appl. Phys.* **96**, 555 (2004).

¹⁶C. B. Parker, J. P. Maria, and A. I. Kingon, *Appl. Phys. Lett.* **81**, 340 (2002).

¹⁷G. A. Smolenksi, *J. Phys. Soc. Jpn.* **S28**, 26 (1970).

¹⁸A. M. Glass, *J. Appl. Phys.* **40**, 4699 (1969).

¹⁹G. Catalan, L. J. Sinnamon, and J. M. Gregg, *J. Phys.: Condens. Matter* **16**, 2253 (2004).

²⁰G. Koster, G. J. H. M. Rijnders, D. H. A. Blank, and H. Rogalla, *J. Appl. Phys.* **74**, 3729 (1999).